Towards Efficient Nuclear Data Uncertainty Quantification in Radiation Shielding Calculations

Juan A. Monleon de la Lluvia,[*,a] Mariya Brovchenko,[a]
Dimitri Rochman,[b] and Eric Dumonteil[c]

[a] *Autorité de Sûreté Nucléaire et de Radioprotection (ASNR)*
PSN-RES/SNC/LN
Fontenay-aux-Roses 92260, France

[b] *Paul Scherrer Institute (PSI)*
Villigen 5232, Switzerland

[c] *Université Paris-Saclay, CEA*
Institut de Recherche sur les Lois Fondamentales de l'Univers
91191, Gif-sur-Yvette, France

[*]Email: juan-antonio.monleondelalluvia@asnr.fr

Number of pages: 42
Number of tables: 11
Number of figures: 12

Abstract

This study explores methodologies for propagating nuclear data uncertainties in radiation shielding calculations. The work is motivated by the aging of Pressurized Water Reactor (PWR) vessels, where quantifying uncertainties can contribute to improved risk assessment; in this context, the present analysis serves as a preliminary step toward more complex, application-specific scenarios. Two approaches are considered: First-Order Second-Moment (FOSM) sensitivity analysis and Monte Carlo Sampling (MCS), both implemented through MCNP6.3. In the FOSM approach, we examine the use of variance reduction in combination with sensitivity calculations, while the MCS method is optimized to address its higher computational demand. Our analysis revealed discrepancies in certain cases when applying variance reduction with sensitivity calculations, which may compromise its applicability under certain conditions. Conversely, the MCS approach, using Sobol and Latin Hypercube Sampling (LHS) with fast Total Monte Carlo or fast GRS techniques, yielded results comparable to FOSM. These findings suggest that using MCS for propagating nuclear data uncertainties in shielding problems should be feasible, while maintaining computational demand similar to that of traditional first-order methods. Future work will test this approach in more complex, realistic configurations.

Keywords — Uncertainty Quantification, Sensitivity Analysis, Monte Carlo Sampling (MCS), First-Order Second-Moment (FOSM), MCNP, Weight Windows

I. INTRODUCTION

Extending the operational lifespan of PWRs relies among other challenges, on an accurate understanding of how structural components respond over time to neutron irradiation. Measurements of neutron flux inside the reactor vessel is usually limited to dosimeters present in the steel samples holder positioned outside the reactor envelop at a specific azimuth, needing the use of detailed simulations that account for complex geometries, multiple materials, and dynamic conditions to evaluate the flux on the vessel [1, 2]. As a result, accurately predicting neutron fluence becomes a key aspect of reactor safety analysis, where uncertainty analysis plays a central role in identifying and quantifying various error sources.

According to the U.S. Nuclear Regulatory Commission [3], uncertainties are divided into two groups. One group consists of systematic errors (epistemic) that influence the fluence prediction in a specific direction. These errors arise from factors such as nuclear data (e.g., transport and dosimeter reaction cross-sections and fission spectra), geometric deviations, variations in material composition, differences in neutron source characteristics, and approximations in the method used. The other group consists of independent random uncertainties (aleatoric) that are combined statistically without regard to any directional bias. Nevertheless, other sources of uncertainty may be present in specific reactor designs or calculational methods.

Monte Carlo simulations serve as a robust tool for modeling the physical processes encountered in nuclear engineering. However, reliable simulation outcomes depend on a comprehensive understanding of inherent uncertainties [4]. Aleatoric uncertainties can be reduced by increasing the number of simulated particle histories or by applying variance reduction techniques, which also improve computational efficiency. In contrast, epistemic uncertainties associated with nuclear data remain linked to the underlying physical processes and are independent of the simulation approach.

While numerous studies have investigated uncertainties in criticality safety assessments [5, 6, 7, 8, 9], research on uncertainty quantification in fluence and shielding calculations is less extensive. Although methodologies have been developed and applied in some cases [10, 11, 12], there remains a need for further comparison and refinement of these methods in the context of radiation shielding.

In this work, we investigate methodologies for nuclear data uncertainty quantification, focusing on neutron flux calculations relevant to radiation shielding applications. While the broader

motivation is related to neutron fluence uncertainties in PWR reactor vessels, the aim here is to assess and compare methodological strategies in a simplified setting. Two approaches are explored: a first-order method based on sensitivity analysis and uncertainty propagation using covariance matrices, and a full-order Monte Carlo sampling technique involving perturbations to nuclear data. The integration of variance reduction techniques in the first-order approach is also examined. By comparing these methods in terms of computational cost and accuracy, we identify their respective strengths and limitations.

The simplified model used in this study is not intended to replicate real-world PWR conditions or provide directly applicable fluence uncertainty results. Rather, it serves as a controlled environment to isolate and evaluate methodological aspects before extending the analysis to more realistic scenarios, such as SINBAD benchmarks or full reactor simulations. It is also worth noting that the current analysis focuses solely on cross section uncertainties. Although this choice aligns with the goal of comparing methodologies, we acknowledge that other nuclear data—such as angular distributions—can significantly influence results in shielding problems. Future work will incorporate these additional sources of uncertainty to move toward a more comprehensive framework.

In what follows, Sec. II presents the model description and the codes employed, while Sec. III provides the background and methodology necessary to understand the first-order and probabilistic approaches used. The results and discussion are presented in Sec. IV, and the main conclusions of the study are summarized in Sec. V.

II. NEUTRONIC SIMULATION

II.A. Codes

MCNP 6.3 [13] is the main transport code used in this study. It is employed to calculate sensitivity coefficients and to run all the simulations needed for the uncertainty quantification through nuclear data sampling.

ADVANTG 3.2.0 [14] is a hybrid code that couples with MCNP simulations to automatically generate variance reduction parameters. It produces a `WWINP` file containing the Cartesian mesh-based weight window values applied during the Monte Carlo simulation. ADVANTG uses DENOVO as its deterministic solver and supports both CADIS (Consistent Adjoint Driven Importance Sampling) [15] and FW-CADIS (Forward-Weighted CADIS) [16] methods. In the CADIS approach, an adjoint transport calculation determines the importance function that guides particle sampling. The FW-CADIS method extends this concept by incorporating the forward flux to optimize responses over the whole spatial grid region defined by the weight windows. While ADVANTG significantly enhances simulation efficiency, it has some limitations: it is limited to fixed neutron source definitions and supports only Cartesian mesh geometries for the weight window.

Serpent 2.2.1 [17] is used for comparing the results from the sensitivity analysis, since it employs a different implementation for calculating sensitivity coefficients. This alternative approach serves as a useful cross-check for the results obtained with MCNP.

FRENDY [18] (FRom Evaluated Nuclear Data librarY to any application) is a nuclear data processing code developed by the Japan Atomic Energy Agency (JAEA) based on the NJOY [19] framework. It adapts many of the established data processing routines from NJOY to read evaluated nuclear data libraries and generate cross section libraries compatible with various transport codes. In this study, only the ACE perturbation file tool of FRENDY was used.

Python was used as the primary tool for processing data. In particular, the CALINS (CALculations and Investigations on Nuclear data uncertainties and Sensitivities) module, developed at ASNR, was used to propagate uncertainties. CALINS applies a first-order matrix propagation method to combine the sensitivities with nuclear data covariance matrices.

II.B. Model and Data Description

Figure 1 illustrates a simplified spherical geometry developed to mimic neutron transport in a PWR environment, tracking the path from the core exit to the reactor vessel and beyond. At the center of the sphere, a neutron point source emits particles with energies ranging from 1 to 3 MeV, approximating the fission spectrum commonly described by a Watt distribution. Moving outward, the configuration consists of successive layers of borated water (10 ppm boron) and 16MND5 steel, all enclosed by air. A 1 cm spherical shell, positioned in the surrounding air, serves as a neutron flux detector (see Table I). The flux is subdivided into three distinct energy groups (0–0.1 MeV, 0.1-1.0 MeV, and 1.0-3.0 MeV) to provide detailed insights into the energy-dependent interactions occurring as neutrons are moderated and scattered by the different materials.

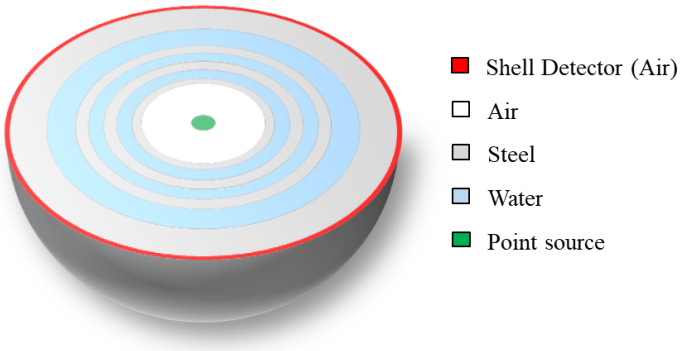

Fig. 1. Schematic Representation of the Sphere's Geometry (not to scale)

Transport calculations use the ENDF/B-VIII.0 nuclear data library with same ACE files across all simulations. Sensitivity coefficients were derived using the SCALE 6.1 44-group energy grid [20]. The associated variance–covariance matrix — constructed from various ENDF/B evaluations and JENDL-3.3 [20] — was used to propagate nuclear data uncertainties. In this procedure, uncertainty propagation included the following reaction channels with their corresponding MT numbers: elastic scattering (MT 2), inelastic scattering (MT 4), radiative capture (n, γ) (MT 102), proton production (n, p) (MT 103), and alpha production (n, α) (MT 107). The present study focuses on the methodology; therefore, the consistency between the nuclear data libraries was not examined here.

Table II details the precise material compositions used in the model, with the isotopes con-

sidered for the sensitivity analysis highlighted in bold. For steel, 10 isotopes accounting for over 98% of its weight fraction were considered.

TABLE I
Layer Specifications of Spherical Geometry

Material	**Inner Radius (cm)**	**Thickness (cm)**
Air	0	162
Steel	162	3
Water	165	5
Steel	170	5
Water	175	6.15
Steel	181.15	6.5
Water	187.65	11.75
Steel	199.4	20
Air/Detector	219.4	1
Air	220.4	79.6

II.C. Variance Reduction in Monte Carlo simulations

Variance reduction methods in Monte Carlo simulations [15] decrease the number of particle histories required to achieve a given statistical precision. Weight windows define acceptable weight ranges based on spatial and energy criteria to guide simulation behavior. Particles exceeding the prescribed window are split into several lower-weight particles, while those falling below may be terminated via Russian roulette. This approach ensures sufficient particle statistics in regions of interest while reducing computational effort in less critical areas, with weights adjusted to preserve the underlying physics. The weight window map allows thus to direct particles toward key regions and to transport them through shielding materials, increasing the probability of particles to reach detectors or other significant locations that might otherwise yield low statistics.

The application of weight windows has been well established in neutron flux calculations for shielding, where they have produced accurate results [21, 22, 23, 24] and compared between different variance reduction methods [25]. However, the application of weight windows in sensitivity analysis is less thoroughly documented. As with any variance reduction strategy, careful consideration is needed to ensure that changes in particle weights or the scoring process do not compromise the underlying physics, which could, in turn, affect uncertainty quantification and sensitivity assessments. Automated tools, such as ADVANTG [14], streamline the creation of weight windows by integrating deterministic transport calculations with Monte Carlo simulations.

TABLE II
Isotopic Composition of Materials in the Model:(a) Water; (b) Air; and (c) Steel. Isotopes Used for Uncertainty Propagation in bold

a

Nuclide	Normalized Atomic Fraction
$^{1}\mathbf{H}$	$\mathbf{6.6666 \times 10^{-1}}$
$^{16}\mathbf{O}$	$\mathbf{3.3333 \times 10^{-1}}$
$^{10}\mathbf{B}$	$\mathbf{1.1054 \times 10^{-6}}$
$^{11}\mathbf{B}$	$\mathbf{4.4495 \times 10^{-6}}$

b

Nuclide	Normalized Atomic Fraction
^{14}N	7.8848×10^{-1}
^{16}O	2.1151×10^{-1}

c

Nuclide	Normalized Atomic Fraction	Nuclide	Normalized Atomic Fraction
^{12}C	9.1261×10^{-3}	$^{56}\mathbf{Fe}$	$\mathbf{8.8106 \times 10^{-1}}$
^{13}C	1.0223×10^{-4}	$^{57}\mathbf{Fe}$	$\mathbf{2.0634 \times 10^{-2}}$
$^{28}\mathbf{Si}$	$\mathbf{3.6398 \times 10^{-3}}$	$^{58}\mathbf{Fe}$	$\mathbf{2.7833 \times 10^{-3}}$
^{29}Si	1.8430×10^{-4}	^{59}Co	2.8212×10^{-4}
^{30}Si	1.2234×10^{-4}	$^{58}\mathbf{Ni}$	$\mathbf{4.1907 \times 10^{-3}}$
^{31}P	1.4314×10^{-4}	$^{60}\mathbf{Ni}$	$\mathbf{1.6014 \times 10^{-3}}$
^{32}S	1.3140×10^{-4}	^{61}Ni	6.9335×10^{-5}
^{33}S	1.0372×10^{-6}	^{62}Ni	2.2027×10^{-4}
^{34}S	5.8221×10^{-6}	^{64}Ni	5.5836×10^{-5}
^{36}S	2.3509×10^{-8}	^{63}Cu	4.8281×10^{-4}
^{50}V	2.7198×10^{-7}	^{65}Cu	2.1489×10^{-4}
^{51}V	1.0852×10^{-4}	^{92}Mo	4.2747×10^{-4}
^{50}Cr	1.1591×10^{-4}	^{94}Mo	2.6861×10^{-4}
$^{52}\mathbf{Cr}$	$\mathbf{2.2327 \times 10^{-3}}$	^{95}Mo	4.5924×10^{-4}
^{53}Cr	2.5314×10^{-4}	^{96}Mo	4.8234×10^{-4}
^{54}Cr	6.2886×10^{-5}	^{97}Mo	2.7727×10^{-4}
$^{55}\mathbf{Mn}$	$\mathbf{1.3618 \times 10^{-2}}$	^{98}Mo	6.9608×10^{-4}
$^{54}\mathbf{Fe}$	$\mathbf{5.5666 \times 10^{-2}}$	$^{100}\mathbf{Mo}$	$\mathbf{2.7727 \times 10^{-4}}$

III. METHODOLOGY

III.A. First-Order Second-Moment Sensitivity Analysis (FOSM)

FOSM [26] sensitivity analysis offers a mathematical framework for quantifying the effects of variations in input parameters on reactor response functions considering only first-order effects. The approach relies on sensitivity coefficients that measure the relative change in a reactor response (e.g., neutron flux) for a given perturbation in an input parameter, combined with covariance matrices that capture the uncertainties and correlations in the nuclear data. Combining these components, uncertainties are propagated under assumptions of linearity of the process and normal distributions of the input and output parameters according to the so-called "Sandwich Formula" [20]:

$$\sigma_{\mathrm{ND}} = \sqrt{S \cdot \mathbf{COV} \cdot S^T} \tag{1}$$

where S is a row vector of sensitivity coefficients and **COV** is the covariance matrix of the nuclear data uncertainties. In its relative form, the sensitivity coefficients are defined as:

$$S_x^R = \frac{\Delta R/R}{\Delta x/x} \tag{2}$$

where R represents the reactor response function and x the perturbed input parameter.

Different techniques are available for implementing FOSM in probabilistic codes. For instance, Generalized Perturbation Theory (GPT) [27], as used in Serpent, combines direct sensitivity from cross section derivatives with indirect sensitivity from flux changes by tracking weighted event perturbations for reaction rate ratios. Alternatively, methods such as Differential Operator Sampling (DOS) [28] and Correlated Sampling (CS) [29] in MCNP, estimate these sensitivity coefficients by directly assessing the impact of small parameter variations on the computed responses.

In our implementation with MCNP, the DOS approach is applied through the use of `PERT` cards, which compute Taylor series coefficients up to second order. The perturbed response $R(p)$ is modeled by

$$R(p) = R_0 + c_1\, p + c_2\, p^2. \tag{3}$$

where R_0 is the unperturbed response, c_1 and c_2 are the first- and second-order Taylor coefficients, and p denotes the applied perturbation. The first-order response can be then used in Eq. 2 to

estimate the sensitivity coefficient.

The full procedure on how to use the `PERT` cards is well explained in [30]. According to its definitions of approximate and exact uncertainties of the perturbed responses, the differences between these two were found negligible in this study. In practice, a separate `PERT` card is required for each combination of isotope, reaction, and energy bin being perturbed. For example, calculating the first-order coefficients for 7 reactions across 14 different isotopes in a 44-group energy structure necessitates $7\times14\times44 = 4312$ `PERT` cards. Recent developments, such as the `FSENS` card [31], have been introduced to compute fixed source sensitivities in a more user-friendly way with promising results; however, these features are not yet available in MCNP6.3 and not accessible to the authors.

For comparison, sensitivity coefficients were also computed using Serpent's GPT implementation, which provides a more direct means to obtain these coefficients. Additionally, integral sensitivity coefficients for the total cross section reaction were evaluated by perturbing the material density directly. Here, the total macroscopic cross section is given by $\Sigma_{tot} = N \cdot \sigma_{tot}$, and sensitivity is determined using the central difference method:

$$S_x^R = \frac{R_{pos} - R_{neg}}{2 \cdot R_0 \cdot (\Delta x/x)} \tag{4}$$

where R_{pos} and R_{neg} are the responses to positive and negative perturbations, respectively.

Variance reduction in MCNP was addressed using two complementary approaches. First, ADVANTG code was used to generate weight windows based on the CADIS method, using the SCALE–6.1 27n19g library for the deterministic calculation and a rectangular 3D mesh with 162 cells in each spatial dimension. Second, the `WWN` card was used to define user-specified weight windows at the level of individual geometrical cells, without energy discretization. The weight in the source cell started at 1 and was halved in each subsequent layer containing either water or steel.

III.B. Monte Carlo Sampling (MCS) for Uncertainty Quantification

MCS methods [32] adopt a probabilistic approach by drawing uncertain input parameters, such as nuclear data, from their probability distributions and performing multiple Monte Carlo simulations. Instead of yielding a single outcome, this method generates a distribution of results from which mean and standard deviation values can be estimated.

A key consideration in this approach is the treatment of correlations among nuclear data parameters. Many parameters (e.g., cross sections) exhibit energy-dependent correlations as well as correlations between different reactions or isotopes. Ignoring such correlations may lead to misleading uncertainty estimates. To address this, both structured sampling techniques and covariance matrix decomposition methods are used. Common sampling strategies include random sampling (RS), Latin Hypercube Sampling (LHS) [33], and low-discrepancy sequences such as Sobol sequences [34]. In RS, pseudo-random numbers are drawn directly from a normal distribution, while LHS and Sobol methods begin with uniformly distributed samples (the former by dividing the cumulative distribution function into equally probable intervals, and the latter by generating a deterministic, low-discrepancy set) and subsequently transforming them into normal values via the inverse cumulative distribution function. Figure 2 illustrates the differences among these sampling strategies.

An important aspect of the sampling process, as shown in the same figure, is the concept of nested sampling. With random sampling, any arbitrary number of samples is expected to cover the entire space. For instance, if 1000 samples are generated, the first 100 samples will typically represent the whole domain, which allows the samples to be divided into multiple non-overlapping sets (e.g., 10 sets of 100 samples each or 1 set of 1000 samples) that individually cover the domain. Similarly, Sobol sequences are constructed in powers of two and have a nested structure. This means that if 1024 samples are generated, one could consider them as 2 sets of 512 or 4 sets of 256, with each set covering the full domain. In contrast, LHS lacks the nested property because it divides each variable's marginal distribution into fixed, equally probable intervals and draws one sample per interval. In its basic form (indeed, augmentation of sample size is supported thanks to complementary algorithms [35]), this structure ensures uniform coverage only for the predetermined sample size, so subdividing a larger set into smaller nested subsets breaks the uniformity. Consequently, LHS is generally applied with a fixed total number of samples.

When dealing with correlated data, these sampling techniques are combined with a transformation based on the covariance matrix to produce samples that maintain the original correlation structure. The covariance matrix, which contains the relationships among the variables, is used to impose the desired correlation on independently generated samples. A key property required for many transformations is that the covariance matrix be positive definite.

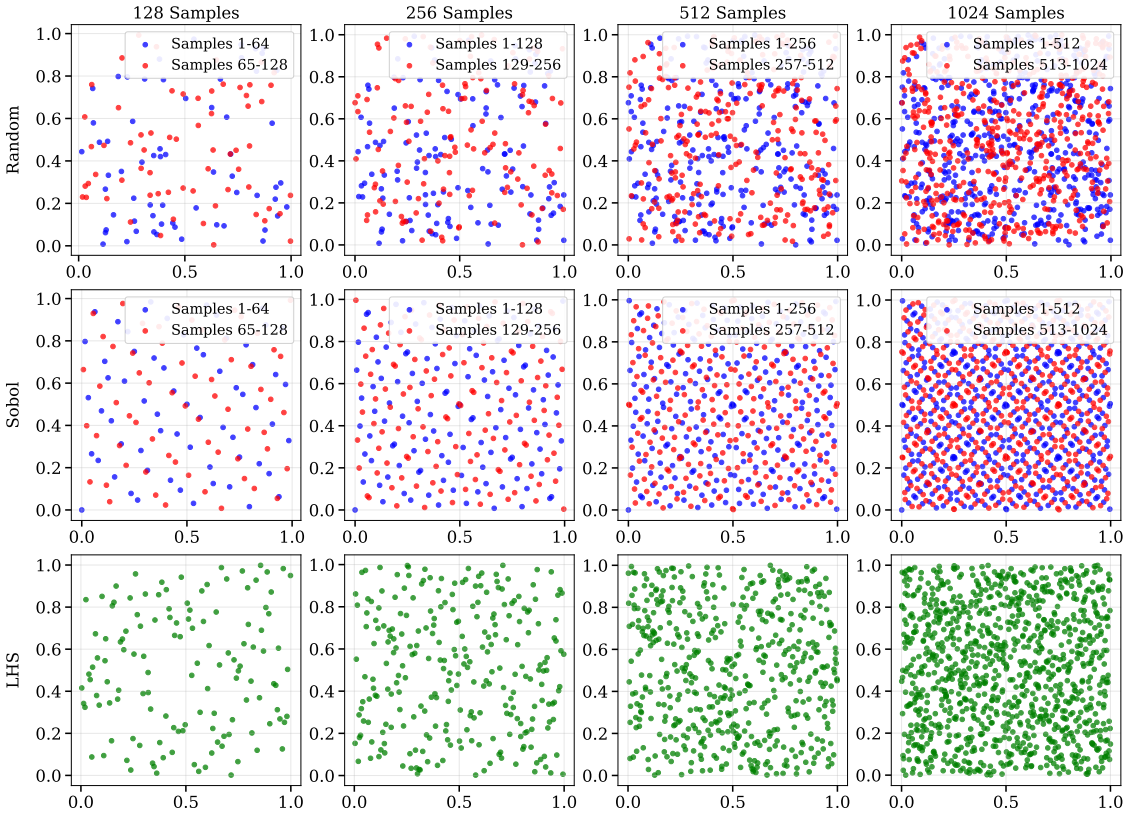

Fig. 2. Comparison of sampling techniques in 2D Space: Random, Sobol, LHS. A well-distributed sampling approach minimizes gaps and ensures better domain coverage.

In our approach, three different matrix decomposition methods were used to factorize the covariance matrix: Singular Value Decomposition (SVD) [36], Eigenvalue Decomposition (EVD) [37], and Cholesky Decomposition [38]. SVD is the most flexible since it does not require the matrix to be positive definite. Eigenvalue decomposition involves representing the matrix in terms of its eigenvalues and eigenvectors, and adjustments need to be made when small negative eigenvalues appear, often due to rounding errors or consistency problems in the matrix. Cholesky decomposition, on the other hand, requires the matrix to be positive definite. In our case, the covariance matrix derived from the SCALE 6.1 44-group structure is an adjusted matrix that may not be strictly positive definite. Therefore, a procedure is implemented to modify the matrix for the sampling, by adjusting its eigenvalues setting those below a small threshold to a small positive number to ensure that it meets the positive definiteness criterion. This process allows for the application of the Cholesky decomposition even when the original matrix does not naturally satisfy strictly

the condition.

By combining each of the three sampling techniques with the three decomposition methods, a total of nine possible combinations were examined. To evaluate the quality of the samples, the Frobenius norm was applied to compare the reconstructed covariance matrix, $\hat{C}$, with the original one, C [39, 40]. Here, the relative error is computed as

$$\varepsilon = \frac{\|C - \hat{C}\|_F}{\|C\|_F}, \tag{5}$$

where the Frobenius norm $\|A\|_F$ for a matrix $A = [a_{ij}]$ is defined as

$$\|A\|_F = \sqrt{\sum_{i,j} a_{ij}^2}. \tag{6}$$

This metric provides a quantitative measure of the agreement between the reconstructed and the original covariance matrices. Detailed results for several key isotopes are presented in Sec. IV. Once the samples are generated, they can be used to produce input files for the ACE perturbation tool in FRENDY [18], enabling the creation of perturbed ACE files to be used in the particle transport calculation.

Building on this foundation, the resulting correlated datasets support a variety of Monte Carlo simulation strategies. In particular, the Total Monte Carlo (TMC) method [10] uses a fixed Monte Carlo seed for all simulations to minimize the probabilistic difference between runs and be able to identify better the effects produced by variations in nuclear data. The nuclear data uncertainty, (σ_{ND}), is estimated via

$$\sigma^2_{\text{observed}} \approx \overline{\sigma^2}_{\text{statistics}} + \sigma^2_{ND} \tag{7}$$

with

$$\overline{\sigma^2}_{\text{statistics}} = \frac{1}{n}\sum_{i=1}^{n} \sigma^2_{\text{statistics},i} \tag{8}$$

where σ_{observed} is the total observed standard deviation from n simulations and $\overline{\sigma}_{\text{statistics}}$ is the average Monte Carlo uncertainty of the individual runs. To ensure that the variations due to nuclear data are clearly recognizable, it is recommended that each run's Monte Carlo uncertainty be kept at roughly 5% of the overall observed uncertainty [10].

In contrast, the Fast TMC [10] approach uses a different Monte Carlo seed for each simulation run. This means that the statistical fluctuations in each run are independent, which allows each individual run to have a higher Monte Carlo uncertainty compared to TMC, without compromising the overall uncertainty estimate. A third strategy, Fast GRS [4], involves running two sets of simulations for each sample using two different seeds. For each sample, let the outputs from the two simulation sets be denoted as $q_i^{(1)}$ and $q_i^{(2)}$ for $i = 1, \ldots, n$. The nuclear data uncertainty is then estimated by computing the covariance between these two sets,

$$\sigma_{ND}^2 = \mathrm{COV}(q^{(1)}, q^{(2)}) = \frac{1}{n-1} \sum_{i=1}^{n} \left(q_i^{(1)} - \overline{q}^{(1)} \right) \left(q_i^{(2)} - \overline{q}^{(2)} \right) \tag{9}$$

where $\overline{q}^{(1)}$ and $\overline{q}^{(2)}$ are the means of the respective simulation sets. Under the assumption that the output variables are identically distributed and conditionally independent, this covariance provides an estimate of the nuclear data uncertainty.

Each of these decisions — choosing the sampling method, selecting the decomposition technique, and adopting a particular simulation strategy — can affect how well the resulting uncertainties represent the true behavior of the system. The sampling method and the number of samples impact how thoroughly the input domain is covered, the decomposition technique influences how accurately both the individual uncertainties and the correlations are reproduced, and the simulation strategy can shape how quickly and accurately the results converge. All of the methods impact the total computational time. In Sec. IV, these approaches are compared and evaluated with respect to their efficiency and accuracy in quantifying uncertainties for the case study at hand.

IV. RESULTS

This section presents the sensitivity analysis results obtained using FOSM and the uncertainty propagation results obtained using both FOSM and MCS. Although a broad range of results has been generated, only the most relevant plots and tables are shown here. In particular, emphasis is placed on the 1.0–3.0 MeV energy range, given its significance in irradiation damage studies. The presented examples reflect the general behavior across multiple isotopes and energy intervals.

IV.A. FOSM Outcomes

IV.A.1. Sensitivity Analysis

Here the results for the sensitivity analysis in MCNP and Serpent are presented. Figure 3 presents a comparison of sensitivity profiles for ^{56}Fe using four simulation approaches: analog MCNP (without weight windows), MCNP with the `WWN` card, MCNP employing ADVANTG-generated weight windows, and Serpent (without any variance reduction). Each plot includes one standard deviation of the statistical uncertainties. Results from the analog MCNP, Serpent, and `WWN` card simulations are generally in agreement, although Serpent occasionally exhibits higher uncertainties for smaller sensitivity coefficients and may report no response for extremely small coefficients (see MT 103 in Figure 3).

For MT 4, however, MCNP did not yield the expected results. Instead of matching the sum of sensitivities from MT 51 to MT 91, the results for MT 4 were found to be approximately seven orders of magnitude lower than anticipated. For this reason, the authors used the sum of the sensitivities of the first two levels (MT 51 and MT 52) instead of the sensitivity to the total inelastic cross section.

A discrepancy in the results is observed when using the ADVANTG-generated weight windows. This discrepancy, which affects individual reaction sensitivities by underestimating elastic reactions and overestimating other reactions, mainly inelastic reactions, ultimately compensates in the total cross section sensitivity. The unperturbed neutron flux remains unaffected by the usage of these weight windows.

To investigate the origin of this discrepancy, several tests were performed. The analysis ruled out the `PERT` cards as a contributing factor, and modifications to ADVANTG parameters,

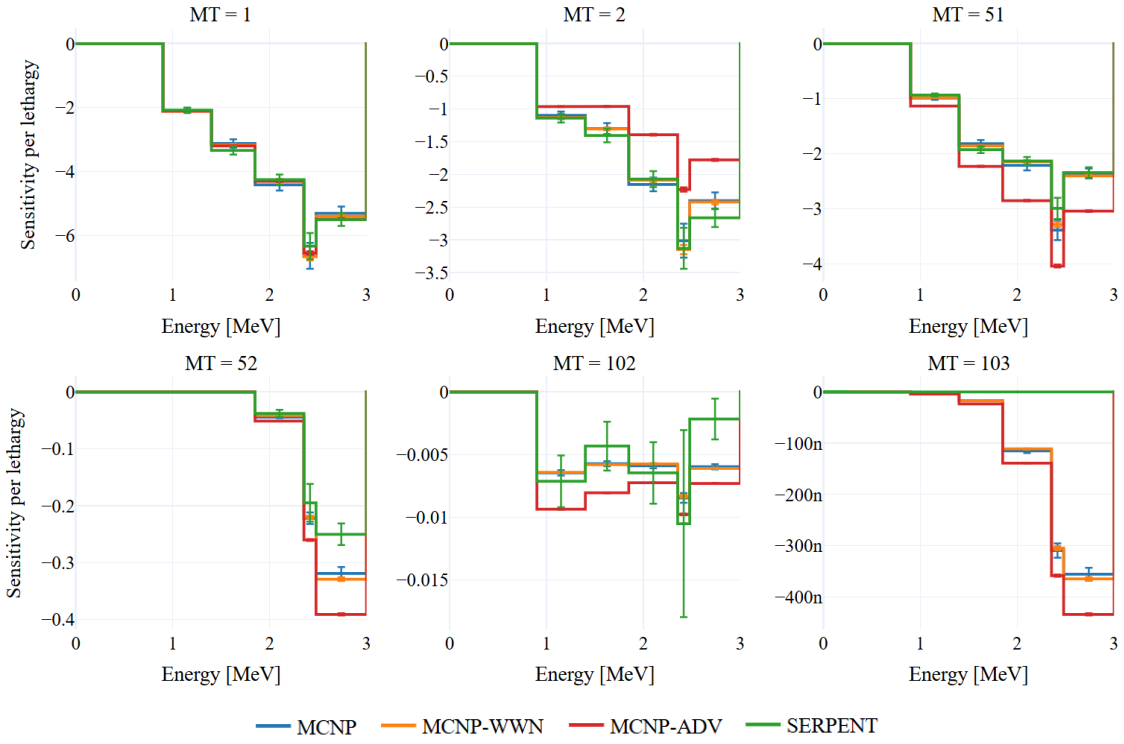

Fig. 3. Sensitivity profiles for Fe-56 reactions: total (MT 1); elastic scattering (MT 2); inelastic scattering to first excited state (MT 51); inelastic scattering to second excited state (MT 51); radiative capture (MT 102); and proton production (MT 103). The x-axis represents the range over which perturbations were applied, and the profiles shows the impact of these perturbations on the detector response for neutrons in the 1–3 MeV range.

including adjustments to the mesh, can improve performance but have no effect in the observed discrepancy. Two dedicated tests were conducted using the same ADVANTG weight window values over identical volumes and within a 27-energy group structure. In one case, the weight windows were applied through the `WWN` card, which restricts their application to the geometry cells. In the other, a super-imposed spherical mesh was defined in the `WWINP` file to match exactly the geometry cells. All other parameters were kept identical. As shown in Figure 4, the difference appears when using the `WWINP` file but not when employing the `WWN` card. These observations suggest that differences in the way MCNP reads and applies weight windows from a `WWINP` file versus through the `WWN` card may be responsible for the discrepancy. Additional testing and discussion on this issue can be found in Appendix A.

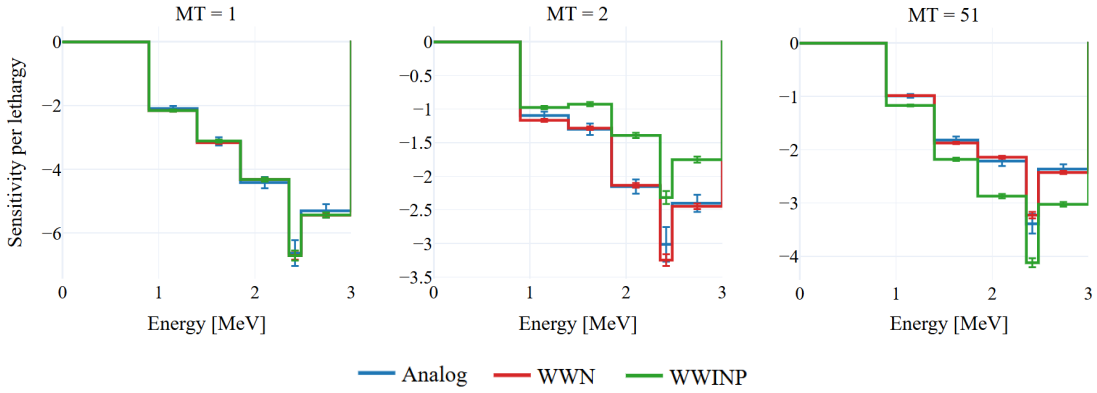

Fig. 4. Sensitivity profiles for Fe-56 reactions: total (MT 1); elastic scattering (MT 2); and inelastic scattering to the first excited state (MT 51). Results compare analog simulations (blue) with simulations using identical weight window values applied via `WWN` (red) and `WWINP` file (green) for neutrons in the 1–3 MeV range.

Figure 5 presents a comparable analysis for ^{1}H. For isotopes that do not experience inelastic scattering, there is no discrepancies, and all four sets of simulations agree. Serpent again reports no response for sensitivities coefficients below a certain threshold (e.g., in the radiative capture channel).

Computationally, the MCNP analog simulation took roughly twice as long as Serpent for the results shown in Figures 3 and 5. Nevertheless, MCNP yielded lower uncertainties, and the number of particle histories that could be run in Serpent was restricted by its considerably higher memory usage, as also reported in previous studies [41, 9].

Comparing the convergence and efficiency of analog MCNP and variance-reduced simulations

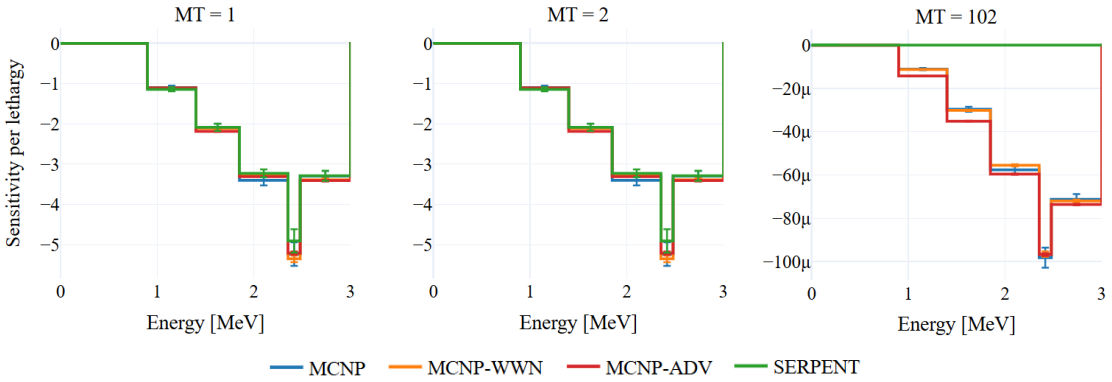

Fig. 5. Sensitivity profiles for ^{1}H reactions: total (MT 1); elastic scattering (MT 2); and radiative capture (MT 102). The x-axis represents the range over which perturbations were applied, and the profiles shows the impact of these perturbations on the detector response for neutrons in the 1–3 MeV range.

shows a marked improvement in key statistical indicators, including the relative error and the Figure of Merit (FOM). Table III illustrates these improvements for a representative case. The FOM is defined as

$$FOM = \frac{1}{\sigma^2 T} \tag{10}$$

where σ is the relative error of the tally result and T is the total simulation run time.

TABLE III
Statistical checks for the first-order Taylor coefficient using the `PERT` card in MCNP for the Fe-56 elastic cross section reaction from 2.479 to 3.0 MeV (nps=1×10^7).

Simulation	**Error**	**VOV**^{*1}	**Slope**	**FOM**
Analog	0.0219	0.0014	4.7	1.6
WWN	0.0067	0.0001	7.4	7.9
ADV-WW	0.0060	0.0000^{*2}	10.0	17

^{*1}Variance of variance.
^{*2}Corresponding to <0.0001 due to digit number limitation.

Energy-integrated total cross-section sensitivities for ^{56}Fe were calculated and compared across the different methodologies. Perturbations were studied for 1%, 2%, 3%, 4%, 5%, and 10%, with 5% results shown in Figure 6, including three standard deviations of the Monte Carlo uncertainties. All methods yield consistent sensitivity coefficients. Within the 1–3 MeV energy range, the neutron flux sensitivity is about twice as large as it is at lower energies.

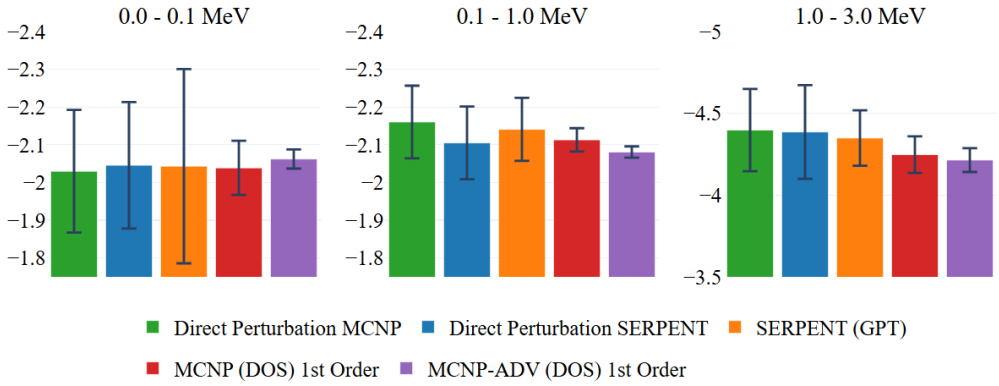

Fig. 6. Sensitivity coefficients for Fe-56 integral total cross section with 5% perturbations.

IV.A.2. First-Order Applicability

A central question when using sensitivity coefficients involves assessing the maximum perturbation magnitude for which linearity still holds. Beyond that, a first-order approach may become inaccurate. MCNP's `PERT` card allows the calculation of both first- and second-order perturbations. Figure 7 shows the perturbed neutron flux as a function of the perturbation in the ^{56}Fe total cross section. Blue lines represents the flux calculated using a first-order approximation, red lines show the flux obtained with first- and second-order approximations and black points correspond to the direct (full-order) perturbation results. Below, the ratio of the approximate results (blue and red) to the direct calculation is displayed, using three standard deviations for the error bars. For this system, linear approximations remain consistent with direct perturbations up to about 5%. Beyond that, significant deviations arise, particularly at higher neutron energies.

A more systematic analysis can be performed using the `PERT` cards to analyze the first-order approximation. To assess this, we evaluate the ratio of the second-order to the first-order contributions of Eq. 3 for each MT and energy bin.

$$\text{Ratio} = \frac{c_2\, p^2}{c_1\, p}, \tag{11}$$

By plotting this ratio as a function of the perturbation across all perturbed MT and energy groups, we can assess the relative impact of the second-order term. A steep slope indicates a stronger influence of the second-order contributions. We then compare these results with the uncertainty values for each reaction channel and energy bin to quantify the specific impact of the

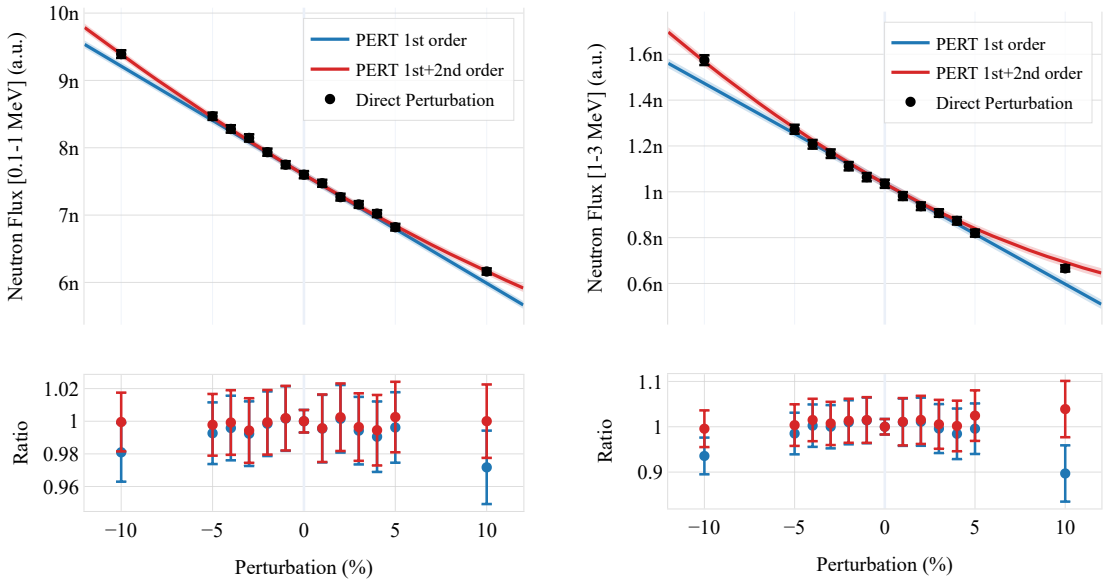

(a) (b)

Fig. 7. Comparison of the perturbed neutron flux for variations in the Fe-56 total cross section computed using first-order (blue), first+second order (red), and direct perturbation (black). Ratio of approximate to direct results shown with 3 standard deviation error bars. (a) 0.1-1 MeV energy range; (b) 1-3 MeV energy range.

second-order effects.

For instance, in the SCALE 44-group covariance matrix for ^{56}Fe, the maximum uncertainties are around 7% for elastic scattering, less than 5% for inelastic scattering, and up to 31% for radiative capture. The analysis shows that elastic and inelastic scattering have the highest sensitivity to second-order effects, with a slope around 1 in the most affected energy bin (see Figure 8). In contrast, the second-order contributions for radiative capture are negligible, with a maximum slope of 3.5×10^{-3}.

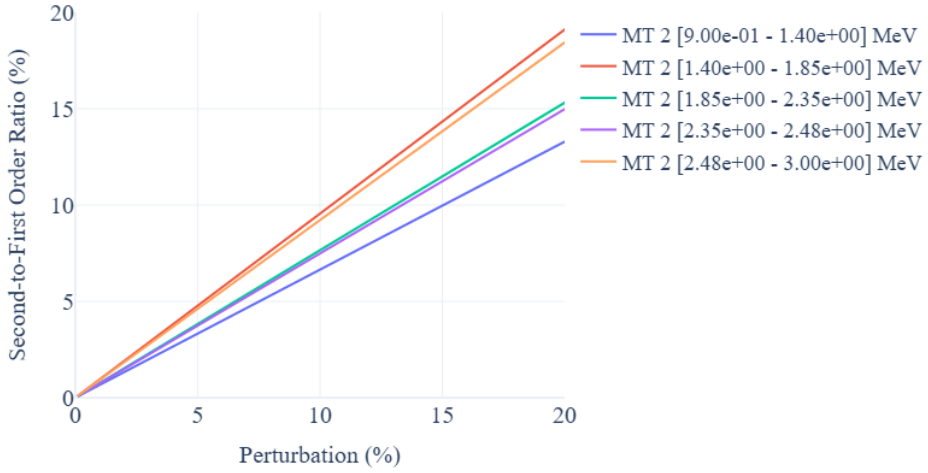

Fig. 8. Second-to-first order ratio for Fe-56 elastic scattering (MT 2) as a function of perturbation for different energy bins.

Given that the maximum uncertainty of the elastic cross section is about 7%, the first-order approximation remains a valid approach.

IV.A.3. Uncertainty Quantification

Uncertainty propagation was carried out by accounting for correlations among energy groups as well as between reactions within the same isotopes when such information was available in the covariance matrix; no cross correlations between different isotopes were considered. Additionally, because the matrix provides data only for total inelastic reactions (MT 4) rather than for specific channels, total inelastic scattering was approximated by combining the sensitivity contributions

from MT 51 and M 52.

Uncertainty propagation used the sensitivity coefficients from the MCNP analog simulation, applying Eq. 1 through python-based CALINS tool. Table IV presents the resulting propagated uncertainties, while Tables V and VI detail the primary contributors to the variance in the 0.1–1 MeV and 1–3 MeV ranges, respectively. As energy increases, the propagated uncertainty rises. The largest contributor to variance is ^{56}Fe, followed by ^{1}H. In the 1–3 MeV range, the top three isotope-reaction pairs account for more than 96.6% of the total neutron flux variance.

TABLE IV
Nuclear data uncertainty for neutron flux by energy ranges.

Detector Energy (MeV)	**Flux per neutron-source**	**Propagated uncertainty (%)**
0-0.1	2.64e-09	5.14
0.1-1.0	7.65e-09	6.51
1.0-3.0	1.07e-09	11.64

TABLE V
Major contributors to the propagated variance in neutron flux between 0.1-1 MeV, with the relative contributions of various isotope-reaction pairs.

Nuclide	**Reaction**	**Integral Sensitivity**	**Relative contribution to the variance (%)**
^{56}Fe	Elastic	-1.28	49.74
^{1}H	Elastic	-3.00	33.15
^{56}Fe	Inelastic	-0.79	10.47
^{16}O	Elastic	-0.69	4.49
^{54}Fe	Elastic	-0.15	1.18

TABLE VI
Major contributors to the propagated variance in neutron flux between 1-3 MeV, with the relative contributions of various isotope-reaction pairs.

Nuclide	**Reaction**	**Integral Sensitivity**	**Relative contribution to the variance (%)**
^{56}Fe	Elastic	-1.97	55.14
^{56}Fe	Inelastic	-2.18	27.70
^{1}H	Elastic	-2.78	13.83
^{16}O	Elastic	-0.22	1.82
^{16}O	Elastic	-0.61	1.11

FOSM typically does not account for the Monte Carlo uncertainty of the calculated sensitivities; insufficient statistics can lead to misleading outcomes. To estimate this effect, a range was established by propagating nuclear data uncertainties using sensitivity coefficients varied by $\pm 1\sigma$, σ being the Monte Carlo uncertainty of the evaluated sensitivity coefficients. Additionally, nuclear data uncertainties were propagated using sensitivity coefficients from simulations with ADVANTG generated weight windows to investigate how the previously observed discrepancy in Sec. IV.A.1, impacts the final propagated uncertainty. Table VII compares these outcomes.

TABLE VII
Propagated nuclear data (ND) uncertainty for different detector energy ranges. Third column shows the uncertainty range corresponding to $\pm 1\sigma_s$, and last column presents the uncertainty using ADVANTG-generated weight windows.

Detector Energy (MeV)	**Propagated ND uncertainty (%)**	**Propagated ND uncertainty $\pm 1\sigma_s$ (%)**	**Propagated ND uncertainty ADV (%)**
0-0.1	5.14	4.79 – 5.51	5.21
0.1-1.0	6.51	6.30 – 6.73	6.35
1.0-3.0	11.64	11.04 – 12.24	11.17

Depending on the detector energy, the propagated uncertainty can vary by relative 5–10%. Although the propagated nuclear data uncertainty computed using sensitivity coefficients from ADVANTG-generated weight windows falls within the $\pm 1\sigma$ band, this apparent agreement seems to result from compensating errors between elastic and inelastic sensitivities. A closer inspection of the contributions from individual isotope–reaction pairs revealed significantly different outcomes, indicating that the overall propagated uncertainty should not be considered reliable.

IV.B. MCS Outcomes

Nuclear data sampling was performed using the same isotopes, reaction channels, and energy bins as in the previous FOSM sensitivity analysis. Relative errors, calculated using Eq. 5, between the reconstructed covariance matrices and the original covariance matrix for ^{56}Fe and ^{1}H, as a function of the number of samples, are summarized in Table VIII. These results indicate that the combination of Sobol sampling with SVD decomposition consistently yields the lowest relative errors across all sample sizes. In the case of ^{56}Fe, where uncertainties are generally higher, the Sobol–SVD approach stands out from the other methods. Among the sampling techniques, Sobol outperforms the alternatives, followed by LHS. Concerning the decomposition methods, aside from

the superior performance of the Sobol–SVD pairing, no significant differences were observed.

TABLE VIII
Relative error for different sampling methods (RS, Sobol, and LHS) and decomposition techniques (SVD, Cholesky, and EVD) for two different cases (Fe-56 and H-1) across varying sample sizes (1024, 512, 256, and 128). The best-performing values for each case are highlighted in bold.

Sampling	**Decomposition**	**Relative Error (%)**							
		Fe-56				**H-1**			
		1024	**512**	**256**	**128**	**1024**	**512**	**256**	**128**
RS	SVD	8.09	15.55	21.55	27.65	0.80	1.68	5.88	4.71
RS	Cholesky	12.00	16.08	20.80	31.05	1.53	5.61	1.07	6.76
RS	EVD	10.11	13.41	20.62	37.12	5.96	0.73	4.56	14.70
Sobol	SVD	**1.36**	**2.33**	**5.20**	**10.28**	**0.05**	0.34	**0.39**	1.16
Sobol	Cholesky	6.67	13.89	18.60	31.14	0.30	0.19	1.96	4.80
Sobol	EVD	5.27	14.72	27.00	39.04	0.68	0.25	0.79	3.00
LHS	SVD	9.25	13.11	17.74	24.90	0.26	**0.10**	0.92	1.87
LHS	Cholesky	9.13	15.03	17.97	29.32	1.34	4.24	1.93	1.78
LHS	EVD	9.37	13.30	20.69	22.53	0.23	0.22	0.80	**0.99**

In the following step, perturbed ACE files were generated with FRENDY and transport calculations were performed using SVD for all three sampling techniques (TMC, fast TMC, and fast GRS). According to [10], to achieve reliable results, TMC requires a Monte Carlo sampling uncertainty of around 5% of the observed uncertainty, while fast TMC can increase this value to around 30% or even 50%. Fast GRS, on the other hand, depends only on the convergence of the mean tally, and in this study it was found that it requires a precision similar to that of fast TMC. To fulfill these requirements, simulations were carried out using different numbers of particle histories (NPS), each yielding different Monte Carlo simulation uncertainties relative to the observed uncertainty. Specifically, a NPS of 1×10^8 achieved around 5%, 1×10^7 around 15%, 1×10^6 about 45%, and 1×10^5 exceeded 100% of the observed uncertainty.

As explained in Sec. III, Sobol and RS allows the obtaining distributions from smaller subsets, whereas LHS does not. Therefore, evaluating LHS for various sample sizes needed additional simulations. In addition, fast GRS needed the performance of two independent sets of simulations because of its method of calculating distributions. Table IX summarizes these simulation efforts and reports the percentage of cases that passed all ten MCNP statistical checks [13]. No variance reduction techniques were used for any of these simulations. The first five simulations were performed in identical conditions except for the use of five different sets of sampled nuclear

data. The behavior of the statistical checks was studied in depth. Simulations conducted with 1×10^5 nps failed most of the statistical checks because the number of particles was insufficient. As the number of particles increased, more statistical checks passed as expected; however, when increasing the particle count over 1×10^7, the slope test began to fail. Despite this, other statistics such as error, VOV, and FOM, showed consistent improvement. Combined with some additional tests, it lead the authors to consider the results of these simulations as reliable.

Additionally, we examined the neutron flux variation for a set of 1024 nuclear data samples to evaluate its conformity to a normal distribution. Figure 9 presents the distribution for ID=1 (see Table IX) along with statistical metrics comparing it to a fitted normal curve. The nominal neutron flux calculated without nuclear data perturbation aligns with the distribution's mean. In addition, skewness and kurtosis values of zero indicate good normal behavior. Despite the Shapiro p-value being very low due to a longer upper tail, the overall distribution is still considered sufficiently close to normal for our analysis.

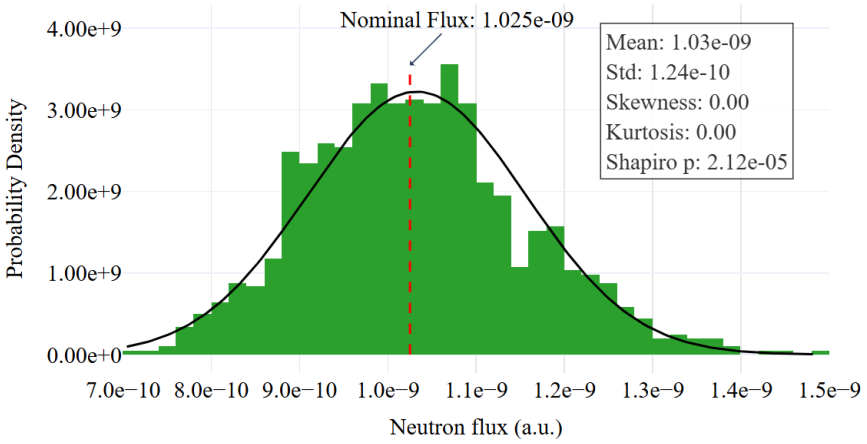

Fig. 9. Distribution of neutron flux values obtained from 1024 samples using Sobol sampling and the Total Monte Carlo (TMC) method with 10^8 particle histories.

Figure 10 compare the nuclear data uncertainties from the different simulation sets for the 1–3 MeV energy range. For clarity, only the most pertinent results are presented. The reference value was calculated by averaging the results from five sets of simulations (IDs 1 to 5 from Table IX). The precision of the reference value is estimated to few percents. For visualization, the plots include a band of ±5% around the reference value. Although the results for the mean values are not shown, convergence was reached more rapidly than the standard deviation and remained

TABLE IX
Summary of MCS Simulations: Comparison of Sampling Methods, Strategies, and Statistical checks

ID	Method	Strategy	NPS	All MCNP Statistical Checks Passed (%)
1	Sobol	TMC	1.00E+08	15.63
2	Sobol	TMC	1.00E+08	15.72
3	Sobol	TMC	1.00E+08	12.60
4	Sobol	TMC	1.00E+08	6.25
5	Sobol	TMC	1.00E+08	31.38
6	RS	TMC	1.00E+08	15.72
7	LHS	TMC	1.00E+08	16.08
8	Sobol	TMC	1.00E+07	88.09
9	RS	TMC	1.00E+07	88.38
10	LHS	TMC	1.00E+07	87.35
11	Sobol	TMC	1.00E+06	70.02
12	RS	TMC	1.00E+06	71.39
13	LHS	TMC	1.00E+06	72.18
14	Sobol	Fast TMC	1.00E+07	88.48
15	RS	Fast TMC	1.00E+07	88.77
16	LHS	Fast TMC	1.00E+07	88.46
17	Sobol	Fast TMC	1.00E+06	84.77
18	RS	Fast TMC	1.00E+06	81.84
19	LHS	Fast TMC	1.00E+06	81.96
20	Sobol	Fast TMC	1.00E+05	2.93
21	RS	Fast TMC	1.00E+05	3.22
22	LHS	Fast TMC	1.00E+05	3.23
23	Sobol	Fast GRS	1.00E+07	89.75
24	RS	Fast GRS	1.00E+07	88.09
25	LHS	Fast GRS	1.00E+07	88.81
26	Sobol	Fast GRS	1.00E+07	92.87
27	RS	Fast GRS	1.00E+07	91.31
28	LHS	Fast GRS	1.00E+07	91.68
29	Sobol	Fast GRS	1.00E+06	70.21
30	RS	Fast GRS	1.00E+06	72.95
31	LHS	Fast GRS	1.00E+06	74.19
32	Sobol	Fast GRS	1.00E+06	92.97
33	RS	Fast GRS	1.00E+06	92.68
34	LHS	Fast GRS	1.00E+06	93.65

consistently within the ±1% range of its reference in all relevant simulations.

In Figure 10(a) the performance TMC method is examined across the different sampling techniques. The outcomes highlight the less efficient performances of the random sampling in comparison to other methods. The limited number of data points available for LHS sampling restricts the ability to ascertain whether the observed behavior is consistently representative or the result of a particularly favorable run. Figure 10(b) displays the effects of reducing the particle count by an order of magnitude.

Figures 10(c) and 10(d) as well as Figures 10(e) and 10(f) display analogous outcomes for the fast TMC and fast GRS cases, respectively. Across all scenarios, Sobol consistently outperforms RS in convergence speed, independently of the number of histories run, while LHS yields robust results. Focusing on the comparison among methods, fast TMC and fast GRS achieve similar outcomes while using ten times fewer particles than TMC. Overall, fast GRS delivers slightly better results than fast TMC, but this difference is likely negligible since fast GRS requires twice as many simulations for the same number of particle histories.

To further extend our analysis, we examined the uncertainty in our results. Bootstrapping was used to calculate the 95% confidence interval for each data point. Figure 11 displays the results for Sobol and LHS sampling across three different numbers of particle histories and the three methods used. For TMC, shown in Figures 11(a) and 11(b), the results demonstrate that when Monte Carlo uncertainty is not sufficiently reduced (i.e., 10^6 particle histories), significant deviations occur. The fast TMC method, illustrated in Figures 11(c) and 11(d), shows that even with 10^5 particle histories, the results remain close to the reference value. However, in these cases, the confidence interval increases substantially to more than ±12%.

To select the most optimal approaches a criterion was established based on computational efficiency and precision requirements. In our study, the precision criteria was arbitrary defined as follows: (1) the reference value must lie within the 95% confidence interval, and (2) the 95% confidence interval must be no more than ±8%. Table X provides a summary of the most efficient parameter combinations for each strategy. Results show that the use of LHS or Sobol for sampling yields equivalent outcomes. Note that RS is omitted from the comparison because its performance was proven inferior to Sobol under the same conditions.

In terms of methodology, several observations can be made in contrast to the findings in [10].

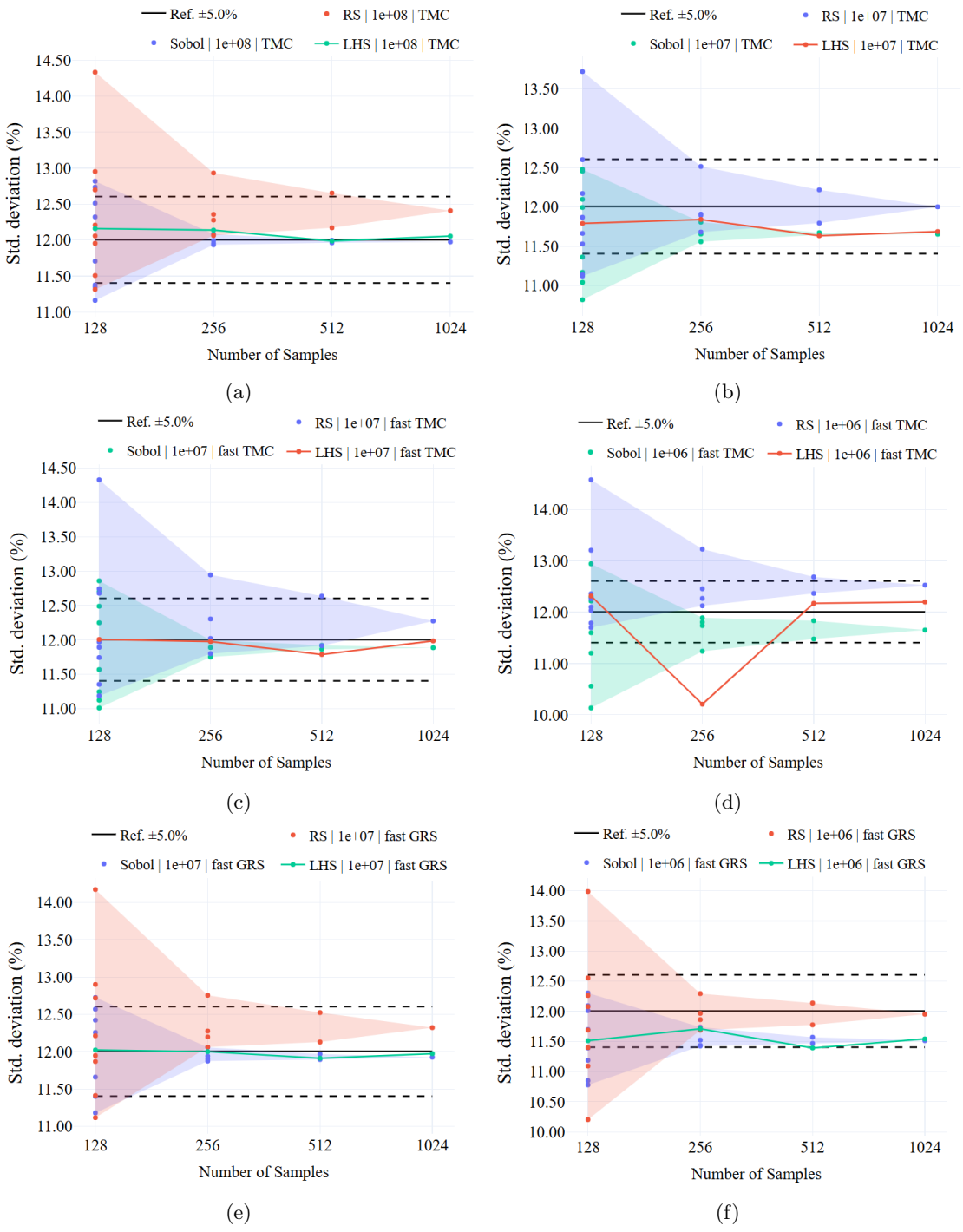

Fig. 10. Evolution of the uncertainty distribution as a function of the number of samples. The results are grouped by simulation strategy: (a), (b) TMC; (c), (d) fast TMC; and (e), (f) fast GRS. Each technique is shown for two different numbers of particle histories.

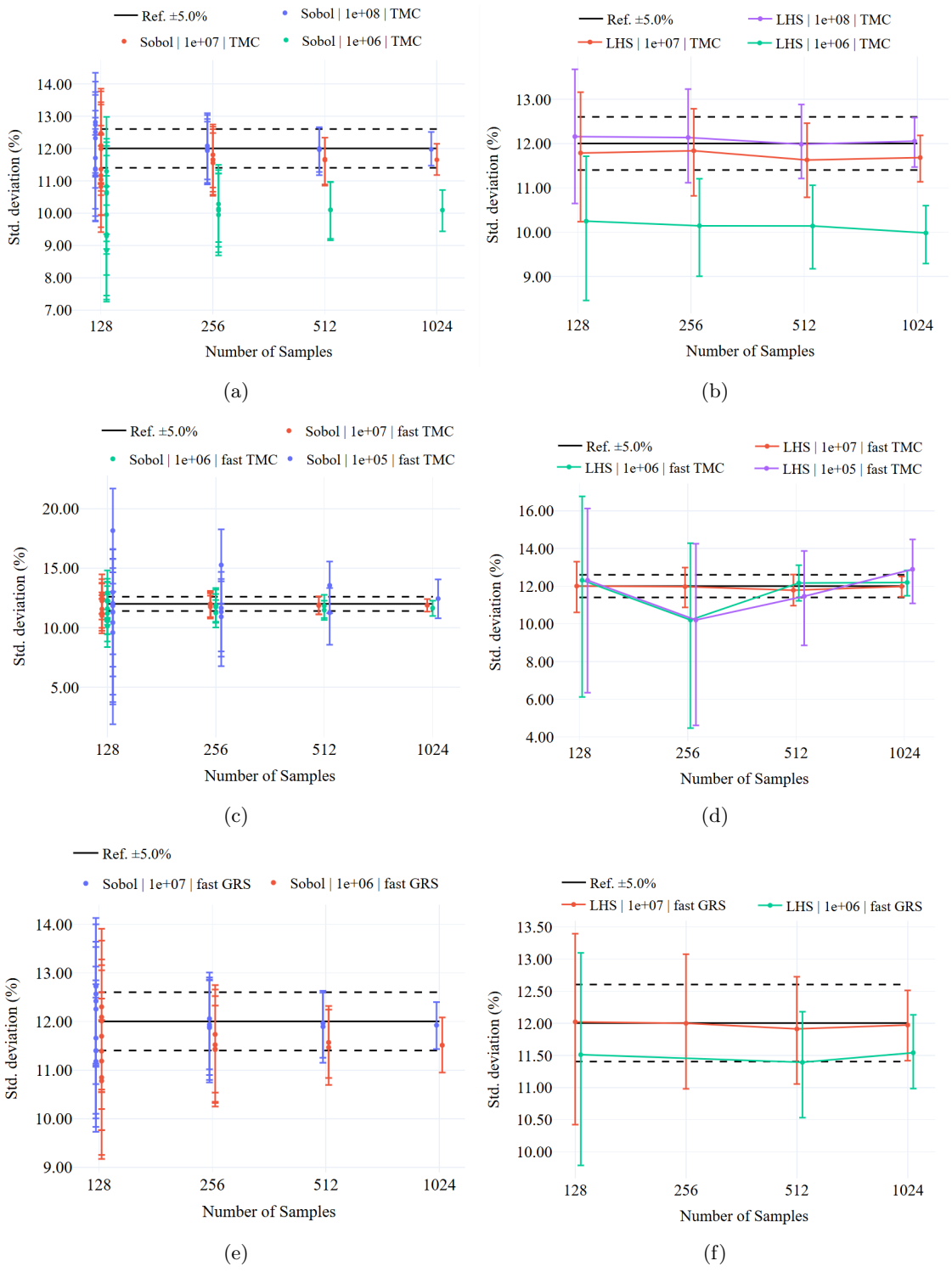

Fig. 11. Evolution of the uncertainty distribution as a function of the number of samples with a 95% CL. The results are grouped by sampling technique and simulation strategy showing the difference for different number of particle histories: (a), (b) TMC; (c), (d) fast TMC; and (e), (f) fast GRS.

TABLE X
Performance Comparison of Efficient MCS Results

Strategy	Total NPS	Sampling Technique	Number of of Samples	ND Std. Deviation (%)	CL at 95%	Relative CL Width (%)
TMC	1.00e+07	Sobol	512	11.67	10.88 – 12.30	6.12
TMC	1.00e+07	LHS	512	11.63	10.77 – 12.44	7.19
Fast TMC	1.00e+06	Sobol	1024	11.65	11.01 – 12.28	5.45
Fast TMC	1.00e+06	LHS	1024	12.19	11.57 – 12.83	5.16
Fast GRS	2.00e+06	Sobol	512	11.52	10.73 – 12.28	6.74
Fast GRS	2.00e+06	LHS	512	11.39	10.54 – 12.21	7.34

First, it is reported that TMC requires approximately 5% Monte Carlo simulation uncertainty relative to the observed uncertainty to trust the results. Our findings indicate that this percentage can increase to 15%, which in our model corresponds to 1×10^7 particle histories, while still providing satisfactory results. On the other hand, Fast TMC is reported to allow the Monte Carlo simulation uncertainty to be between one-third and one-half of the observed value. This aligns with our results, which yield acceptable performance for approximately 45% Monte Carlo simulation uncertainty relative to the observed value. A similar level of precision is observed for Fast GRS, that requires roughly half the number of samples compared to Fast TMC, but double the number of simulations.

Regarding computational cost, Fast TMC and Fast GRS are comparable, whereas TMC requires approximately five times more resources.

IV.C. Final Comparison of Uncertainty Propagation Methods

Finally, Table XI compares the propagated uncertainty between using both the FOSM and MCS approaches across all energy ranges. For this analysis, we used the MCS results obtained with fast TMC and Sobol sampling from Table X, along with the reference values from MCS calculated using simulations 1-5 from Table IX. Overall, the uncertainty estimates from both methods agree well with the reference values. Although minor differences are observed, they remain within the uncertainty bounds, indicating that both approaches reliably capture the propagated uncertainties.

Assessing the computational and engineering efforts required by FOSM and MCS for propagating nuclear data uncertainties is challenging due to the strong dependence on problem complexity and target precision, and while optimizing computational cost was one of the main focuses

TABLE XI
Comparison of Nuclear Data Uncertainty Propagation via FOSM and MCS (Fast TMC - Sobol - 1e+06 histories) Methods

Detector Energy (MeV)	**Ref. Uncertainty (%) (95% CL)**	**MCS Uncertainty (%) (95% CL)**	**FOSM Uncertainty (%) [$\pm 1\sigma$]**
0–0.1	5.26 (5.16 – 5.36)	5.06 (4.75 – 5.34)	5.14 (4.79 – 5.51)
0.1–1.0	6.56 (6.44 – 6.84)	6.59 (6.26 – 6.88)	6.51 (6.30 – 6.73)
1.0–3.0	12.00 (11.77 – 12.22)	11.65 (11.01 – 12.28)	11.64 (11.04 – 12.24)

when implementing the MCS methodology, such optimization for FOSM was not initially within the scope of this study. This makes a direct comparison even more difficult; nonetheless, some indicative remarks on computational cost are shared to provide a general sense based on the simulations conducted here.

The MCNP manual [13] notes that each additional `PERT` card can increase running time by 10–20%, with the exact impact varying with the problem. In fact, this study found that the running time changed by a factor of four when shifting from perturbing isotopes in water to perturbing isotopes in steel. As highlighted in [30], although adding extra `PERT` cards does not always cause a large increase in runtime, the total number required, determined by the number of isotopes, reactions, and energy group structures, can grow rapidly if not properly controlled, potentially resulting in significant longer simulations or the exclusion of less influential contributors to the propagated uncertainty, thereby increasing the overall error.

In contrast, MCS allows for the inclusion of numerous reactions and isotopes without directly impacting the simulation runtime. Under an efficient MCS configuration (i.e. using 1×10^6 particle histories with fast TMC and 1024 samples), the Monte Carlo transport simulations required fewer computational resources than FOSM. For the results presented in Table XI (excluding the reference values), MCS used approximately one-fourth of the resources needed for FOSM. This efficiency gain depends on the number of isotopes perturbed in the FOSM approach, where each isotope was simulated separately using five different `PERT` methods. The computational cost gap could likely be reduced by perturbing all isotopes in a single run with only two `PERT` cards for first- and second-order results. Additionally, FOSM offers a more direct means to decompose the contributors to propagated uncertainty, whereas MCS involves the extra step of creating perturbed ACE files, which adds further computational costs.

V. CONCLUSION

This paper presented an in-depth study of methodologies for propagating nuclear data uncertainties for a fixed source calculation within a simplified spherical model. The objective was to identify the most appropriate method for application in computationally intensive problems, such as PWR shielding calculations. Two widely used approaches were considered: first-order second-moment sensitivity analysis (FOSM) and Monte Carlo Sampling (MCS). The FOSM method propagates uncertainties via Eq. 1, relying on first-order approximations of sensitivity coefficients in conjunction with the covariance matrix, whereas MCS perturbs the nuclear data library files and performs separate simulations for each perturbed instance to obtain a distribution from which statistical quantities can be estimated.

Various aspects of each methodology were evaluated. For the FOSM approach, comparisons between the MCNP and Serpent codes demonstrated good agreement, with each using a different implementation to calculate the sensitivity coefficients. Serpent offers an attractive approach for performing a first-order perturbation analysis by providing all required results within a single simulation, although its high memory consumption may impose practical limitations. In contrast, MCNP demands additional post-processing yet offers a broader range of information, including up to second-order perturbations. This additional detail is particularly beneficial for verifying the linearity of the problem and confirming the suitability of a first-order approximation.

Additionally, two methods for implementing variance reduction using weight windows were tested. While the optimization of variance reduction techniques is model-dependent and the present model did not require substantial efficiency improvements to obtain acceptable statistics, the study aimed to assess the compatibility of these techniques with sensitivity calculations. It was found that, in the cases considered, employing the `WWINP` file to define weight windows showed inconsistencies in the sensitivity coefficients of individual reactions, thereby raising concerns regarding the applicability of the FOSM methodology in variance reduction–dependent models.

For the MCS approach, efforts were made to identify the most efficient approach to reliably estimating the uncertainties of nuclear data, thereby reducing the computational demand inherent to this method. Optimization efforts addressed several aspects, including sampling techniques (Random Sampling, Latin Hypercube Sampling, and Sobol sequences), decomposition methods for the covariance matrix (Singular Value Decomposition, Eigenvalue decomposition, and Cholesky

decomposition), strategies employed for MCS (TMC, fast TMC, and fast GRS), as well as the number of samples and the Monte Carlo simulation uncertainty of each individual run necessary for convergence. The results indicate that both Sobol and LHS sampling consistently yield more reliable outcomes than RS under identical conditions, with no notable differences between the various decomposition methods. In terms of efficiency, fast GRS with 512 samples and fast TMC with 1024 samples produced accurate results within a $\pm 8\%$ confidence interval at 95%, with each individual run having approximately 45% Monte Carlo uncertainty relative to the total observed uncertainty.

Overall, the propagated uncertainties obtained from FOSM and MCS are in strong agreement, consistent with its reasonably linear behavior. Differences between both methods are expected to become more pronounced for models exhibiting nonlinear behavior. The detailed convergence analysis performed, which provided explicit uncertainty ranges for both methods, supports the authors' consideration that, depending on the number of parameters involved, the computational demand for uncertainty quantification using MCS may not necessarily exceed that of FOSM. While FOSM relies on first-order approximations and may not always be suitable for comprehensive uncertainty quantification, its sensitivity analysis remains useful for identifying the most influential input parameters. In general, FOSM can effectively propagate nuclear data uncertainties to the neutron flux, provided that: (1) weight-window parameters do not alter sensitivity coefficient calculations; (2) the problem exhibits sufficient linearity to justify a first-order approximation; and (3) uncertainties associated with angular distributions and other nuclear data can be considered negligible, as their sensitivities cannot be computed in MCNP using `PERT` cards and are therefore excluded from the FOSM framework. These latter uncertainties could be propagated within a Monte Carlo Sampling approach provided covariance data is available for them. When the above conditions are not met, MCS remains the preferable option.

CREDIT STATEMENT

Conceptualization: JM, MB, DR

Data curation: JM

Formal analysis: JM

Funding acquisition: MB

Investigation: JM

Methodology: JM, MB

Project administration: MB

Software: JM

Resources: MB, DR

Supervision: MB, DR

Validation: JM, MB, DR

Visualization: JM

Writing – original draft: JM

Writing – review & editing: MB, DR, ED

ACKNOWLEDGMENTS

The authors have no acknowledgments to declare.

DISCLOSURE STATEMENT

No potential conflict of interest was reported by the authors.

DATA AVAILABILITY

Study materials and data for this study can be made available at request.

A. APPENDIX A: SLAB-GEOMETRY TEST FOR WEIGHT WINDOW DISCREPANCY

A simplified 300 cm long slab was modeled to study why the sensitivity coefficients show discrepancies when ADVANTG weight windows are applied through the `WWINP` file. The same

layered materials and the sequence of the spherical model were linearly arranged along the x direction, with a homogeneous unidirectional neutron source distributed over the volume between $x = 0$ and $x = 0.1$, emitting in the range 1 to 3 MeV. Cross-sectional dimensions (e.g., 40 cm×40 cm, 1 cm×1 cm, and others) were varied to see how transverse size might affect the results. MCNP 6.3 was used to calculate reaction-specific sensitivity coefficients (focusing on elastic and inelastic scattering) in a detector region defined after the last steel layer and coefficients being calculated via `PERT` cards.

Many tests were performed, while three of them are presented below. First, a purely analog simulation ran without weight windows. Second, the ADVANTG-generated weight window values were provided through a `WWINP` file aligned with the geometry cells so that each cell received a set of energy defined weight-window values. Third, the same ADVANTG-generated values were applied using the `WWN` card. Since the weight window mesh and the geometrical cells were perfectly aligned, we could directly convert these values into the `WWN` format and the same energy group structure was used for both cases. Figure 12 shows that, despite using identical data, the `WWINP` approach produced a discrepancy in sensitivity coefficients for larger cross sections (e.g., 40 cm×40 cm or 100 cm×100 cm), while the `WWN` approach did not. When the slab's cross section was reduced to 1 cm×1 cm, the discrepancy disappeared resulting in an overlap with analog and `WWN` results. Further refinement of the mesh in the `WWINP` file did not resolve the difference, suggesting it is not simply a meshing artifact.

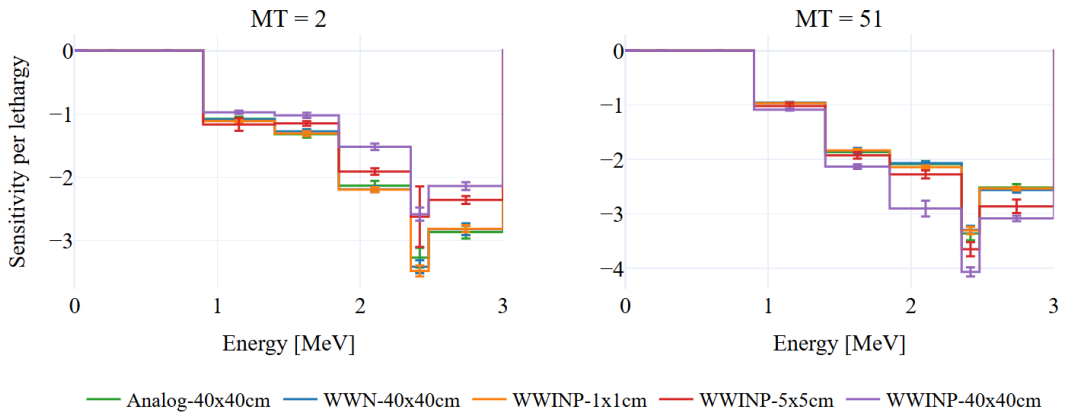

Fig. 12. Results on Slab-Geometry test for weight window discrepancy.

The main observations can be summarized as follows:

- Simulations without weight windows or using `WWN` do not show abnormal results.
- Adjusting ADVANTG parameters (such as the transverse mesh) did not allow to remove the discrepancy.
- Changing the moment where particle weight is checked, either at surface crossing or collision, did not have effect on the results.
- The discrepancy with `WWINP` increases up to around $20\,\mathrm{cm}^2$ but shows little to no further growth beyond this, with results for $40\,\mathrm{cm}^2$ and $100\,\mathrm{cm}^2$ being nearly identical.
- Unperturbed neutron flux is not affected by the discrepancy.

Our study showed that switching from `WWN` to `WWINP` led to discrepancies in sensitivity coefficients for the spherical and slab geometries. In the slab geometry, reducing the cross-sectional dimensions (e.g., to $1\,\mathrm{cm}\times1\,\mathrm{cm}$,) causes the bias to disappear. It remains to be seen whether a similar effect might occur in cylindrical geometries, such as those found in PWR shielding problems. Early results suggest that converting the ADVANTG weight window values into the `WWN` format could be a promising solution to explore further.

REFERENCES

[1] S. F. d'Energie Nucleaire (SFEN), "The vessel fluence," URL https://inis.iaea.org/records/f0h6w-m9711.

[2] N. Thiollay, "Validation de la fluence reçue par la cuve," URL https://cea.hal.science/cea-02614139, journée Technique SFEN "Poursuivre le fonctionnement des réacteurs nucléaires après 40 ans".

[3] U. S. Nuclear Regulatory Commission. Office of Nuclear Regulatory Research, "Regulatory Guide 1.190 Calculational and Dosimetry Methods for determining Pressure Vessel Neutron Fluence," URL http://catalog.gpo.gov/F/?func=direct&doc_number=000630223&format=999, medium: Language material, Electronic resource, Computer, Online resource.

[4] W. Zwermann, B. Krzykacz-Hausmann, L. Gallner, M. Klein, A. Pautz, and K. Velkov, "Aleatoric and Epistemic Uncertainties in Sampling-Based Nuclear Data Uncertainty and Sensitivity Analyses," .

[5] O. Leray, H. Ferroukhi, M. Hursin, A. Vasiliev, and D. Rochman, "Methodology for core analyses with nuclear data uncertainty quantification and application to Swiss PWR operated cycles," **110**, 547; 10.1016/j.anucene.2017.07.006., URL https://www.sciencedirect.com/science/article/pii/S0306454916311288.

[6] D. Rochman, A. Dokhane, A. Vasiliev, H. Ferroukhi, and M. Hursin, "Nuclear data uncertainties for core parameters based on Swiss BWR operated cycles," **148**, 107727; 10.1016/j.anucene.2020.107727., URL https://www.sciencedirect.com/science/article/pii/S0306454920304254.

[7] A. Albà, A. Adelmann, and D. Rochman, "Uncertainty quantification of spent nuclear fuel with multifidelity Monte Carlo," **211**, 110892; 10.1016/j.anucene.2024.110892., URL https://www.sciencedirect.com/science/article/pii/S0306454924005553.

[8] D. Huang, U. Mertyurek, and H. Abdel-Khalik, "Verification of the sensitivity and uncertainty-based criticality safety validation techniques: ORNL's SCALE case study,"

361, 110571; 10.1016/j.nucengdes.2020.110571., URL https://www.sciencedirect.com/science/article/pii/S0029549320300662.

[9] C. Jin, S. Liu, S. Zhang, J. Liang, and Y. Chen, "Nuclear Data Sensitivity and Uncertainty Study for the Pressurized Water Reactor (PWR) Benchmark Using RMC and SCALE," **15**, *24*, 9511; 10.3390/en15249511., URL https://www.mdpi.com/1996-1073/15/24/9511, number: 24 Publisher: Multidisciplinary Digital Publishing Institute.

[10] D. Rochman, W. Zwermann, S. C. v. d. Marck, A. J. Koning, H. Sjöstrand, P. Helgesson, and B. Krzykacz-Hausmann, "Efficient Use of Monte Carlo: Uncertainty Propagation," **177**, *3*, 337; 10.13182/NSE13-32., URL https://doi.org/10.13182/NSE13-32, publisher: Taylor & Francis _eprint: https://doi.org/10.13182/NSE13-32.

[11] A. Vasiliev, D. Rochman, M. Pecchia, and H. Ferroukhi, "Exploring Stochastic Sampling in Nuclear Data Uncertainties Assessment for Reactor Physics Applications and Validation Studies," **9**, *12*, 1039; 10.3390/en9121039., URL https://www.mdpi.com/1996-1073/9/12/1039, number: 12 Publisher: Multidisciplinary Digital Publishing Institute.

[12] S. Chen, D. Bernard, and P. Blaise, "Attenuation of neutron and photon-induced irradiation damage in pressurized water reactor pressure vessels," **145**, 107601; 10.1016/j.anucene.2020.107601., URL https://www.sciencedirect.com/science/article/pii/S0306454920302991.

[13] LANL, "MCNP Code Version 6.3.0 Theory & User Manual," .

[14] S. W. Mosher, A. M. Bevill, S. R. Johnson, A. M. Ibrahim, C. R. Daily, T. M. Evans, J. C. Wagner, and J. O. Johnson, "ADVANTG An Automated Variance Reduction Parameter Generator," ; 10.2172/1105937., URL http://www.osti.gov/servlets/purl/1105937/.

[15] A. Haghighat and J. Wagner, "Monte Carlo variance reduction with deterministic importance functions," **42**, 25; 10.1016/S0149-1970(02)00002-1.

[16] J. C. Wagner, E. D. Blakeman, and D. E. Peplow, "Forward-Weighted CADIS Method for Variance Reduction of Monte Carlo Calculations of Distributions and Multiple Localized Quantities," .

[17] J. Leppänen, "Serpent – a Continuous-energy Monte Carlo Reactor Physics Burnup Calculation Code," .

[18] K. Tada, R. Kondo, T. Endo, and A. Yamamoto, "Development of ACE file perturbation tool using FRENDY," **60**, *6*, 624; 10.1080/00223131.2022.2130463., URL https://doi.org/10.1080/00223131.2022.2130463, publisher: Taylor & Francis _eprint: https://doi.org/10.1080/00223131.2022.2130463.

[19] R. Macfarlane, D. W. Muir, R. M. Boicourt, I. I. I. Kahler, and J. L. Conlin, "The NJOY Nuclear Data Processing System, Version 2016," ; 10.2172/1338791., URL https://www.osti.gov/biblio/1338791.

[20] W. Wieselquist and R. A. Lefebvre, "SCALE 6.3.1 User Manual," ; 10.2172/1959594., URL https://www.osti.gov/biblio/1959594.

[21] M. Brovchenko, B. Dechenaux, K. W. Burn, P. C. Camprini, I. Duhamel, and A. Peron, "Neutron-gamma flux and dose calculations in a Pressurized Water Reactor (PWR)," **153**, 05008; 10.1051/epjconf/201715305008., URL https://www.epj-conferences.org/articles/epjconf/abs/2017/22/epjconf_icrs2017_05008/epjconf_icrs2017_05008.html, publisher: EDP Sciences.

[22] T. Goričanec, B. Kos, K. Ambrožič, A. Trkov, L. Snoj, and M. Kromar, "Determination of neutron flux redistribution factors for a typical pressurized water reactor ex-core measurements using Monte Carlo technique," **11**; 10.3389/fenrg.2023.1137867., URL https://www.frontiersin.orghttps://www.frontiersin.org/journals/energy-research/articles/10.3389/fenrg.2023.1137867/full, publisher: Frontiers.

[23] R. Vuiart, M. Brovchenko, J. Taforeau, and E. Dumonteil, "A Detailed Analysis of the H.B. Robinson-2 Reactor Pressure Vessel Dosimetry Benchmark," **15**, *14*, 5098; 10.3390/en15145098., URL https://www.mdpi.com/1996-1073/15/14/5098.

[24] A. Vasiliev, H. Ferroukhi, M. Pecchia, D. Rochman, A. Laureau, V. Lamirand, and A. Pautz, "Revision of PSI calculation capabilities and validation experience on the BEPU-type reactor dosimetry applications," **308**, 03011; 10.1051/epjconf/202430803011., URL https://www.epj-conferences.org/articles/epjconf/abs/

2024/18/epjconf_isrd-17_03011/epjconf_isrd-17_03011.html, publisher: EDP Sciences.

[25] M. Brovchenko, L. Tillard, K. W. Burn, B. Cochet, and A. Jinaphanh, "On the use of different variance reduction techniques within MCNP to calculate the flux on the concrete walls of a pressurized water reactor," .

[26] A. Haldar and S. Mahadevan, *Probability, Reliability and Statistical Methods in Engineering Design*, vol. 23, John Wiley & Sons, Inc.URL https://linkinghub.elsevier.com/retrieve/pii/S0167473000000254, ISSN: 01674730 Issue: 1 Journal Abbreviation: Structural Safety.

[27] M. Aufiero, A. Bidaud, M. Hursin, J. Leppänen, G. Palmiotti, S. Pelloni, and P. Rubiolo, "A collision history-based approach to sensitivity/perturbation calculations in the continuous energy Monte Carlo code SERPENT," **85**, 245; https://doi.org/10.1016/j.anucene.2015.05.008., URL https://www.sciencedirect.com/science/article/pii/S0306454915002650.

[28] J. A. Favorite, "An Alternative Implementation of the Differential Operator (Taylor Series) Perturbation Method for Monte Carlo Criticality Problems," **142**, *3*, 327; 10.13182/NSE02-A2311., URL https://doi.org/10.13182/NSE02-A2311, publisher: Taylor & Francis _eprint: https://doi.org/10.13182/NSE02-A2311.

[29] B. C. Kiedrowski, "Review of Early 21st-Century Monte Carlo Perturbation and Sensitivity Techniques for k -Eigenvalue Radiation Transport Calculations," **185**, *3*; 10.1080/00295639.2017.1283153., URL https://www.osti.gov/pages/biblio/1438213, institution: North Carolina State University, Raleigh, NC (United States) Publisher: Taylor & Francis.

[30] J. Favorite, "Using the MCNP Taylor series perturbation feature (efficiently) for shielding problems," **153**, 06030; 10.1051/epjconf/201715306030., URL http://www.epj-conferences.org/10.1051/epjconf/201715306030.

[31] J. R. Lamproe, T. E. Cutler, M. Y. Hua, J. D. Hutchinson, M. E. Rising, S. D. Clarke, and S. A. Pozzi, "Preliminary verification of the MCNP perturbation and fixed-

source tally sensitivity tools," **194**, 110040; 10.1016/j.anucene.2023.110040., URL https://www.sciencedirect.com/science/article/pii/S0306454923003596.

[32] A. J. Koning and D. Rochman, "Towards sustainable nuclear energy: Putting nuclear physics to work," **35**, *11*, 2024; 10.1016/j.anucene.2008.06.004., URL https://www.sciencedirect.com/science/article/pii/S0306454908001813.

[33] N. Balakrishnan, "Latin Hypercube Sampling," *Methods and Applications of Statistics in the Atmospheric and Earth Sciences*, 140–143, John Wiley & SonsGoogle-Books-ID: vbWkgKJCcDAC.

[34] I. M. Sobol, D. Asotsky, A. Kreinin, and S. Kucherenko, "Construction and Comparison of High-Dimensional Sobol' Generators," 16; 10.1002/wilm.10056., URL https://www.researchgate.net/publication/264591156_Construction_and_Comparison_of_High-Dimensional_Sobol'_Generators.

[35] M. Stein, "Large Sample Properties of Simulations Using Latin Hypercube Sampling," **29**, *2*, 143; 10.2307/1269769., URL https://www.jstor.org/stable/1269769, publisher: [Taylor & Francis, Ltd., American Statistical Association, American Society for Quality].

[36] K. Lange, "Singular Value Decomposition," K. Lange (Editor), *Numerical Analysis for Statisticians*, 129–142, Springer; 10.1007/978-1-4419-5945-4_9., URL https://doi.org/10.1007/978-1-4419-5945-4_9.

[37] K. Lange, "Eigenvalues and Eigenvectors," K. Lange (Editor), *Numerical Analysis for Statisticians*, 113–128, Springer; 10.1007/978-1-4419-5945-4_8., URL https://doi.org/10.1007/978-1-4419-5945-4_8.

[38] K. Lange, "Linear Regression and Matrix Inversion," K. Lange (Editor), *Numerical Analysis for Statisticians*, 93–111, Springer; 10.1007/978-1-4419-5945-4_7., URL https://doi.org/10.1007/978-1-4419-5945-4_7.

[39] T. T. Cai, C.-H. Zhang, and H. H. Zhou, "Optimal rates of convergence for covariance matrix estimation," **38**, *4*; 10.1214/09-AOS752., URL http://arxiv.org/abs/1010.3866.

[40] X. Cui, C. Li, J. Zhao, L. Zeng, D. Zhang, and J. Pan, "Covariance structure regularization via Frobenius-norm discrepancy," **510**, 124; 10.1016/j.laa.2016.08.013., URL https://www.sciencedirect.com/science/article/pii/S0024379516303500.

[41] P. Griveaux, M. Hursin, I. Kodeli, D. Leichtle, and A. Pautz, "Computation of sensitivity coefficients in fixed source simulations with SERPENT2," **200**, 114191; 10.1016/j.fusengdes.2024.114191., URL https://www.sciencedirect.com/science/article/pii/S0920379624000450.